Post glacial lithospheric flexure and induced stresses and pore pressure changes in the northern North Sea

Balz Grollimund*, Mark D. Zoback
Department of Geophysics, Stanford University, Stanford, CA 94305, USA

Abstract

We have compiled data on the least principal stress, overburden, pore pressure and stress orientation for 92 wells in the northern North Sea. These data show that the least principal stress is close to the overburden in the Tampen Spur indicating high horizontal stress in this area. Closer to the coast, i.e. east of the Viking Graben the least principal stress drops significantly. Along with this spatial change in stress magnitudes, the orientation of the maximum horizontal stress rotates from ≈100° in the Tampen Spur to ≈80° around block 35/9. Analytical and numerical models of plate flexure suggest that these observed lateral stress variations are the result of deglaciation, superimposed on a regional stress field dominated by ridge push.

The pore pressure in the northern North Sea roughly follows the stress trend, i.e. high overpressures where horizontal stresses are high (Tampen Spur) and close to hydrostatic pore pressures east of the Viking Graben where stresses are decreased. This close relationship of pore pressure and horizontal stress suggests that they have the same source. We have modeled the pore pressure change expected from the poroelastic response to deglaciation. The results show that strong overpressures in the Tampen Spur appear to be only partly caused by deglaciation and flexure. Other sources of overpressure, such as compaction disequilibrium also play an important role.

Keywords: stress; pore pressure; glacial rebound; North Sea; boreholes; lithosphere

* Corresponding author. Tel.: +1 (650) 725 5831; Fax: +1 (650) 725 7344; E-mail: balz@geo.stanford.edu

1. Introduction

Many previous studies have investigated the effect of glaciation on the lithosphere (e.g. Walcott, 1970; Peltier, 1976; James and Bent, 1994; Wu, 1997). Most of these studies for Fennoscandia were based on uplift data (e.g. Fjeldskaar, 1997), on the occurrence of earthquakes (e.g. Wolf, 1987; Klemann and Wolf, 1998; Johnston et al., 1998), or on the analysis of gravity anomalies (Ekman and Makinen, 1996) which allowed them to come up with estimates for certain parameters such as the asthenospheric viscosity and lithospheric thickness. Direct investigation of the influence of glaciation-deglaciation on the mechanics of the crust-mantle system requires knowledge of the in-situ stress field within the crust. Rough estimates for the stress state in the crust of Fennoscandia come from the analysis of earthquake focal plane mechanisms (Bungum, 1989; Gregersen et al., 1991; Lindholm et al., 1995). However, to accurately investigate possible stress changes caused by lithospheric flexure, it is necessary to have direct stress measurements to calibrate and test the models. Fortunately, the northern North Sea contains numerous hydrocarbon wells which can provide appreciable data for such an analysis. In this study, we used data from 92 wells located between 61°N and 62°N (Fig. 1).

The northern North Sea is an ideal area to investigate flexural stresses due to deglaciation. We used borehole breakout data from the World Stress Map project (Müller et al., 1992; Zoback, 1992) and drilling induced tensile fractures (Wiprut and Zoback, 1998) to monitor the orientation of the maximum horizontal stress (S_{Hmax}). Fig. 1 shows that the azimuth of S_{Hmax} changes from >100° west of the Viking Graben to ≈80° on the east side of the Viking Graben, indicating that the stress field in the northern North Sea is subjected to significant spatial variations possibly related to post glacial flexure. Other indications of flexural stress perturbations in the northern North Sea are the increased earthquake activity in this area (Fig. 1), and the variations of stress magnitudes as described below.

2. Observed stress in the northern North Sea

In this study we focus on the relatively detailed data collected along the cross section shown in Fig. 1, although stress data have been compiled throughout the Norwegian sector of the North Sea (Grollimund et al., in press). We have compiled leak-off tests (LOT) to determine the magnitude of the least principal stress (S_3), and density logs to calculate the vertical stress (S_v). A LOT is performed by pressurizing a short, uncased section of a well until a hydraulic fracture opens and begins to take fluid. By plotting the pressure as a function of mud volume pumped into the hole, a deviation from a linear trend indicates the onset of fracture opening and gives a rough estimate for S_3. To be independent of depth, we used the normalized least principal stress (S_3/S_v) to characterize the stress field and its spatial variations. If S_3/S_v approaches 1, then S_3 is close to S_v which by definition characterizes a reverse faulting environment, according to Anderson faulting theory (Anderson, 1951). Of course, another possibility for $S_3/S_v \approx 1$ is an almost isotropic stress state. However, at least for depths > 5 km numerous earthquakes in the northern North Sea suggest a stress state close to failure of the crust, thus precluding an isotropic stress state. Furthermore, the stress analysis of Wiprut and Zoback (1998) shows that a high horizontal stress anisotropy exists in the Visund field. Accordingly, $S_3/S_v \approx 1$ most probably indicates high horizontal stresses, i.e. strike-slip to reverse faulting in the northern North Sea, whereas decreased S_3/S_v imply lower horizontal stresses, i.e. strike-slip to normal faulting. Thus, we believe S_3/S_v is a good general indicator of the magnitude of horizontal stress.

For this analysis, we used data from wells from the hydrocarbon fields in the Tampen Spur (e.g. Snorre, Gulfaks, Visund), and other fields east of the Viking Graben (e.g. Fram, block 35/9). Some wells didn't have a sufficient number of leak-off tests to allow S_3 to be estimated with depth. For such cases, we merged data from nearby wells, assuming that the stress field is relatively uniform between the wells. Data points which don't lie exactly on the cross section were projected perpendicular onto it.

Using basic error propagation, the uncertainty associated with S_3/S_v $\Delta(S_3/S_v)$ is equal

to the sum of the relative errors of S_3 and S_v. The relative errors are defined as $\Delta S_3/S_3$ for the least principal stress, and $\Delta S_v/S_v$ for the vertical stress. While the determination of S_v is very precise (ΔS_v=0.5 MPa), the S_3 estimates have a maximum error of ±2 MPa (Grollimund et al., in press). As S_v and S_3 increase with depth the relative error decreases with depth and consequently $\Delta S_3/S_v$ is on the order of ±0.1 at a depth of 1000 m and ±0.05 at a depth of 3000 m.

Fig. 2a shows the results of the S_3/S_v-analysis along part of the cross section illustrated in Fig. 1 as a function of depth below sea level. In the Tampen Spur S_3/S_v is close to 1 at depths greater than 1000 m MSL. Towards the coast S_3/S_v drops to ≈0.8 at a depth of ≈2500 m MSL. At depths shallower than 1000 m MSL no change of S_3/S_v is observable along the entire cross section. The transition from high S_3/S_v ratios in the Tampen Spur towards decreased values closer to the coast occurs in the vicinity of the Viking Graben, over a horizontal distance of ≈100 km. The lateral distance of the stress change will be important later on, to estimate the lithospheric thickness. With respect to the error, even if S_3/S_v has an uncertainty of ≈0.05 at a depth of 2,500 the observed spatial variation is 0.2 or even higher slightly to the north (Fig. 3a). As a result, the observed spatial stress variation is above the noise level associated with the stress measurements.

In summary, the northern North Sea consists of two main stress provinces, (1) the Tampen Spur with high S_3/S_v ratios indicating high horizontal stresses, i.e. a strike-slip to reverse faulting stress state, and (2) the area between the Viking Graben and the coast with decreased S_3/S_v ratios (≈0.8) suggesting decreased horizontal stresses, i.e. strike-slip to normal faulting. Additionally, Wiprut and Zoback (1998) have estimated the magnitude of S_{Hmax} from the analysis of wellbore failure in the Visund field. For depths between 2000 m and 3000 m MSL they predict S_{Hmax} magnitudes that are considerably higher than S_v (S_{Hmax}/S_v≈1.25) (Fig. 2a), supporting a strike-slip to almost reverse faulting stress regime.

To interpret the stress field it is crucial to know the pore pressure (P_p) as stress and pore pressure are closely related. Also, the faulting behavior of rock depends on the stress

state and the pore pressure (e.g. Jaeger and Cook, 1979). P_p data comes from the same boreholes as the S_3 and the S_v measurements. The majority of pore pressures are derived from repeat formation tests (RFT), which are routinely performed at reservoir depth. An RFT is carried out by measuring the fluid pressure necessary to prevent flow into or out of the formation. Additionally, drill stem tests provide a limited number of P_p measurements. Similar to the S_3 analysis, we display pore pressure normalized by S_v (P_p/S_v). For typical S_v with depth profiles in the northern North Sea, P_p/S_v ratios of ≈0.5 indicate approximately hydrostatic pore pressures. P_p/S_v-values higher than 0.5 indicate overpressured formations.

The errors associated with the pore pressure measurements are very small (≈0.2 MPa). As a consequence, $\Delta(P_p/S_v)$ is on the order of ±0.04 at shallow depth and decreases to values of less than 0.02 at depths of 2500 m or below which compared to the observed variations of P_p/S_v is negligible.

Fig. 2b shows P_p/S_v as a function of depth along the same cross section as Fig. 2a. To a depth of 2500 m MSL, P_p/S_v hardly exceeds 0.5, which implies that the pore pressure is hydrostatic to this depth. The slight increase in P_p/S_v towards the coast at shallow depth is not the result of higher P_p but rather of a decreased overburden due to increased water depth. However, between 2000 m and 3000 m MSL a distinct zone of overpressure develops west of the Viking Graben with P_p/S_v of up to 0.8. At the same depth P_p is still close to hydrostatic between the Viking Graben and the coast, with the exception of a slightly overpressured zone at a depth of 2000 m MSL.

The lateral stress variations described above are not limited to the northern North Sea but are rather a large scale phenomenon that can be observed throughout the North Sea. I.e. S_3/S_v is generally approaching unity at distances greater than 100 km from the coast (e.g. in the Tampen Spur) but is decreased in the vicinity of the coast (Fig. 3a). Conversely, with the exception of the Tampen Spur P_p is mostly hydrostatic (Fig. 3b).

3. Flexural stresses

As a next step, we attempt to explain the observed stress variations in the northern North Sea. Several authors have pointed out the influence of ridge push on the regional stress field along the entire Norwegian margin (e.g. Gregersen et al., 1991; Müller et al., 1992). Since the crust cools down and becomes denser as it moves away from the Mid Atlantic Ridge, gravitational sliding occurs and causes high stresses in the direction of increasing plate age and thickness (e.g. Forsyth and Uyeda, 1975; Parsons and Richter, 1980; Bott and Kusznir, 1984). Ridge push uniformly increases stress over large areas. However, Figs. 1-3 show that the observed stress changes in the northern North Sea occur over a horizontal distance of ≈100 km which suggests that an additional stress source affects the local stress field.

Goelke (1996) modeled stress perturbations as a result of the interaction between ridge push and a laterally heterogeneous crustal structure. However, another typical cause of such stress variations within short distances is bending of the lithosphere due to the isostatic response to loads imposed on the surface of the lithosphere. Thus, in this paper we investigate lithospheric flexure as an alternative mechanism to explain the local stress perturbations observed in the northern North Sea. The Baltic ice sheet that also covered parts of the northern North Sea until ≈15,000 years ago (e.g. Mangerud, 1979; Andersen, 1981; Lundqvist, 1986) represented a significant load on the lithosphere. Assuming an ice sheet thickness of 1000 m or more, an imposed vertical load of ≈10 MPa would result. Another possibility for such a load is the accumulation of sediments which were deposited in the northern North Sea, especially during the Tertiary (Dore, 1992). However, according to Stein et al. (1989) sedimentation occurs over a very long period (millions of years) and the associated flexure stresses most likely disappeared as a result of creep processes within the crust. Conversely, the melting of the ice sheet as a relatively recent phenomenon and consequently the crust had no time to relax the induced bending stresses. Therefore, for the remainder of this paper we will only consider the perturbation of stresses in the

northern North Sea that are the result of glacial loading and unloading.

Fig. 4 illustrates two simplified end-member models on how glacial loading cycles are expected to perturb the local stress field, assuming that the entire lithosphere behaves as a rheologically uniform plate (Stephansson, 1988, Stein et al., 1989). In the case of Fig. 4a the ice sheet existed for a long enough time for the lithosphere to relax the induced bending stresses. For this assumption, subsequent melting of the ice sheet leads to extension under the former ice sheet and compression away from it, at shallow depth. At the base of the lithosphere the stress perturbations are inverted, i.e. compression under the former ice sheet and extension away from it. For this case the magnitude of the stress perturbation increases as the lithospheric rebound progresses. Stein et al. (1989) use this assumption to explain the transition from reverse faulting earthquakes offshore Baffin Bay to normal faulting earthquakes along the coast. Stephansson (1988) proposes the opposite assumption. That is, none of the bending stresses relax during the existence of the ice sheet (Fig. 4b). For this case, we would expect increased stresses under the former ice sheet and a stress decrease further offshore, at shallow depth. The stress perturbation decreases during the lithospheric rebound and completely vanishes after the rebound is complete.

In addition to the bending stresses discussed in the previous paragraph, the change from a bent lithosphere before ice melting to a flat lithosphere after complete rebound causes a net shortening in both models illustrated in Fig. 4. This effect does not cause variations in horizontal stress magnitudes either spatially or with depth but instead leads to a uniform horizontal stress increase throughout the entire lithosphere.

Both end-member models are able to explain the observed decrease in horizontal stress at shallow depth (<5 km) towards the coast as illustrated in Figs. 2a and 3a). The model illustrated in Fig. 4b requires that the ice sheet front was predominantly located in proximity of the coast to explain the decreased horizontal stresses east of the Viking Graben. On the western side of the Viking Graben this model appropriately suggests a horizontal stress increase as lithospheric bending tapers off. Conversely, for the model

illustrated in Fig. 4a the ice front must have been mainly located in the vicinity of the Viking Graben to fit the stress observations by actively increasing the horizontal stresses west of the Viking Graben and decreasing them towards the coast.

The occurrence of numerous thrust faulting earthquakes west of the Viking Graben seems to favor the model in Fig. 4a as this model predicts an increase in horizontal stress for this area rather than decreased stresses as proposed by the model in Fig. 4b. Instead, this model suggests that earthquake occurrence is promoted immediately east of the coast line which is not observed. Further, the model in Figure 4a implies that bending-induced stress perturbations increase with ongoing lithospheric rebound whereas the other end-member model suggests that the stress perturbations disappear with the completion of lithospheric rebound. Uplift data show that postglacial uplift is approaching its completion (Ekman and Makinen, 1996), so the model from Fig. 4b would suggest that most of the stress perturbation has disappeared. The increased earthquake occurrence in the northern North Sea and the marked spatial change in measured stress across the Viking Graben imply that there is an appreciable stress perturbation. Consequently, the model proposed by Stein et al. (1989) seems to fit the observations better, suggesting that creep processes within the lithosphere are capable of significantly relaxing stresses on a time scale that is comparable to the duration of glaciation.

Realistically, the lithosphere is strongest in the upper crust as elevated temperatures at great depths enable stress relaxation as a result of creep processes. Consequently, the observed stresses most likely reflect a combination of both end-member models, i.e. the lower part of the lithosphere relaxes while the upper part stores the imposed bending stresses. We will revisit this issue in Section 3.3 by using a finite element model to combine a purely elastic upper crust with a viscoelastic lower crust and lithospheric mantle in order to study the interaction between different rheologies. First, we will investigate under what conditions a single layer lithosphere is capable of reproducing the observed stresses to set the stage for the multi-layer model in Section 3.3.

3. 1. Analytical model for glacial loading

We have used a simple analytical model derived by Nadai (1963) for the bending of a viscoelastic slab under a distributed load to explore the effects of different lithospheric thicknesses (T) and relaxation times (τ) on the evolution of bending stresses within a single-layer lithosphere after loading of the ice sheet. In this model, the lithosphere has a Maxwell-viscoelastic rheology and a constant thickness. The viscoelastic lithosphere is underlain by a fluid substratum which allows the lithosphere to be in isostatic equilibrium. The boundaries of the model are subjected to the condition that the first derivative of the deflection is zero. See Appendix A for a formal description of the model.

For this simple model we are assuming that the ice sheet grew instantaneously at the beginning of the Pleistocene, i.e. 2 million years ago, and that it always had the same extent as 15,000 years ago. In the numerical model, we will use a more refined ice model as compiled by Andersen and presented by Denton and Hughes (1981) based on the mapping of ice front features. For now we model the ice sheet as a 1 km thick block that covered the entire Horda Platform and ended east of the Viking Graben where ice front features are very abundant (Andersen, 1981), suggesting that the ice sheet remained at this stage during large portions of its existence. A transition in the magnitude of shale compaction across the Viking Graben further supports this assumption (Hansen, 1996). Obviously, during its existence the ice sheet was subjected to cycles of growth and retreat. In this section, we are not interested in the exact ice sheet history but rather in a rough estimate of its overall effect on the lithosphere which can be mimicked well enough by a constant reference ice sheet extent. However, in Section 3.3 we will also consider cyclic ice loading.

Fig. 5 shows modeled stress perturbations for different lithospheric thicknesses and relaxation times. We assumed values of T=50 km and T=30 km as they result in stress perturbations with wavelengths comparable to the observations (Figs. 2 and 3). The upper graphs for each subplot show bending stresses at the surface with different lines

representing different time slices. The line with the largest magnitude displays the instantaneous response after growing of the ice sheet. Subsequent lines represent the time evolution of the bending stresses with an increment size of 200,000 years. The lower part of each subplot shows modeled stress perturbations as a function of depth, after 2 Ma of ice loading. Fig. 5a and b show that for $\tau=10^5$ years most of the bending stresses that were induced by the growing of the ice have relaxed almost entirely after a relatively short period. Certainly, 2 Ma into the existence of the ice sheet remaining stress magnitudes are not higher than 3 MPa for T=50 km and 4 MPa for T=30 km respectively. As a result of the block-shaped ice sheet, the bending stresses are antisymmetric with respect to the ice front. Also, note that the wavelength of the stress perturbations depend on T as well as on time, i.e. the wavelength of the stress perturbation always decreases with time and that higher T cause larger wavelengths. Even for a higher $\tau=10^6$ years (Fig. 5c, d), which is probably more realistic, a large portion of the induced stress perturbation relaxes. In the case of T=50 km (Fig. 5c) the stress perturbation decreases by up to 20 MPa west of Snorre and the remaining stresses are not higher than 10 MPa. For T=30km and τ=1 Ma the remaining stress variations are up to 13 MPa but are more confined laterally than for T=50km.

According to this simplistic model, large parts of the stress perturbations induced by glacial loading have disappeared before the melting of the ice sheet even for a relatively high τ of 1 Ma. Thus, the model favors the assumption made in Fig. 4a, which is also supported by the observed stress data.

3. 2. Analytical model for glacial unloading

Based on the arguments presented above, we now assume that the bending stresses induced by glacial loading were significantly reduced before the ice sheet started to melt. Since the melting of the last ice sheet occurred relatively recently (≈15,000 years ago) we further assume that the lithospheric response to glacial unloading was fully elastic and the

ice sheet has a rectangular shape (see Fig. 6). The resulting horizontal stress perturbations after the complete rebound of the lithosphere are displayed in Fig. 6. Note, that the different lines in Fig. 6 represent different lithospheric thicknesses rather than time slices as in Fig. 5. The model predicts an E-W stress increase in the fields of the Tampen Spur and decreased horizontal stresses in proximity of the coast. The amplitude of the stress perturbation is on the order of 20 MPa, depending on the assumed value of T. As mentioned earlier, the observed stress decrease occurs over a horizontal distance of ≈100 km. The result for T=30 km best matches this observed wavelength and T=40 km still gives a satisfactory fit to the lateral extent of the observed stress drop, whereas T=20 km clearly results in a too short stress pulse.

In summary, the comparison of observed data and the elastic unloading model suggest an effective elastic thickness of 30 to 40 km on a timescale of ≈10,000 years for the lithosphere in the northern North Sea, which agrees well with the findings of Fjeldskaar (1997) who proposes T<50 km. However, the amplitudes of the predicted stress perturbations (≈20 MPa) are upper bounds, since we have to assume that no stress perturbation existed prior to ice melting and that the lithospheric rebound after glacial unloading is complete. The analysis of gravity data shows that the rebound is only completed by ≈80% (Ekman and Makinen, 1996).

With these analytical models we only investigated the perturbation of bending stresses in proximity of the ice sheet edge. By doing so, we expect a tendency from high to low horizontal stresses towards the coast which corresponds to the observed transition from reverse/strike-slip to strike-slip/normal faulting. However, the modeled stress perturbation is spatially constrained and negligible at distances larger than 100-150 km from the ice front. In fact, underneath the center of the former ice sheet, i.e. further onshore, earthquakes and movements of postglacial faults suggest a thrust faulting stress state (e.g. Muir Wood, 1989), which is most likely due to the net shortening of the lithosphere as mentioned in Section 3.

3. 3. Numerical model of the entire loading-unloading cycle

Clearly, by analytically modeling the lithosphere as a single layer we ignored the fact that the lithospheric rheology varies with depth. For example, the assumption that the entire lithosphere, even at shallow depth, relaxes deviatoric stresses might be overly simplified. Also, the analytical models are incapable of including time-varying ice sheet geometries. For these reasons we used the finite element technique to first model a full ice loading-unloading cycle with varying ice sheet geometries and later include cyclic ice loading, on a rheologically more realistic lithosphere.

Fig. 7a shows the basic setup of the two-dimensional numerical model. It covers the cross section illustrated in Fig. 1, which corresponds to a lateral extent of 600 km. With depth, the model consists of a 20 km thick elastic upper crust, made up of 5 km of sediments and 15 km of basement, and a 15 km thick viscoelastic lower crust to account for ductile processes that occur at this depth. The depth of the transition to the ductile layer (lower crust) is based on estimates from studies of geothermal gradients (Dragoni et al., 1993). We assign the lower crust a viscosity of 10^{22} Pa s which Strehlau and Meissner (1987) infer for a feldspar/pyroxene-dominated, wet lower crust. The lithospheric mantle is 15 km thick and has a viscosity of 10^{23} Pa s. The lithosphere system is underlain by an asthenosphere which is modeled as a semi-infinite viscous substratum with a viscosity that results in the best match with the observed land uplift ($3x10^{19}$ Pa s) (see also Table 1). More specifically, at the lithosphere-asthenosphere interface we apply a pressure that is proportional to the vertical deflection. The proportionality constant corresponds to the density restoring force (k) which we introduced in the analytical models (see Appendix A). The purpose of this load is to give the lithosphere the ability to reach isostatic equilibrium after ice loading, and to obtain lithospheric rebound following the onset of ice melting. Additionally, we apply a pressure that is proportional to the rate of vertical deflection on the lithosphere-asthenosphere interface. The proportionality constant is the viscosity of the asthenosphere. Thus, the asthenosphere prevents the lithosphere from deforming

instantaneously after ice emplacement but with time the viscous resistance of the asthenosphere decreases and the density restoring force starts to compensate for the ice load until the viscous resistance disappears and isostatic equilibrium is reached. Ice melting causes the same effect but in the opposite direction.

The modeled lithosphere consists of bilinear 4-node elements which means that strain within an element changes linearly in both directions. The model has a lateral resolution of 1 km in the center, and 2 km towards the ends while the vertical resolution is 1 km for the upper crust, and 1.5 km for the lower crust and the lithospheric mantle. Thus, the model is resolved by 40 elements vertically, and 350 elements horizontally resulting in a total number of 14,000 elements. Even the sediment part of the upper crust which is the thinnest rheological unit vertically consists of 5 element layers. The model assumes plane strain perpendicular to the modeled cross section, and the ends of the cross section are fixed horizontally but are allowed to move vertically.

Before we use the numerical model for a full loading cycle we wanted to check whether element sizes and boundary conditions were chosen appropriately. We reproduced the results of the analytical unloading model with a lithospheric thickness of 30 km. As the lithospheric thickness of the numerical model is 50 km we scale Young's Modulus (E) such that the flexural rigidity (D) of the numerical model corresponds to the flexural rigidity of the analytical model. The dashed line in Fig. 6 displays the flexural stress obtained from the numerical solution, demonstrating that the elastic response of the numerical model has a maximum error of ≈1 MPa.

The model with one full loading cycle starts 1.1 Ma ago with an isotropic stress state, i.e. S_{Hmax} and S_{hmin} are equal to S_v. By assuming an initially isotropic stress state we are ignoring the fact that the crust might have been prestressed, e.g. as a result of ridge push. However, the assumption of initially isotropic stresses allows us to focus on the stress changes deglaciation may have induced. Fig. 7b illustrates the temporal evolution of the modeled ice sheet. 1.1 Ma ago we let the ice sheet grow to its lateral extent and thickness

at 15,000 years ago and let the ice geometry unchanged for one million years until 110,000 years ago. This phase of the model aims to mimic the Pleistocene cold climate with frequent ice sheet advances and retreats. The ice sheet extent from 15,000 years ago is probably a good average of the ice sheet's geometry during this phase as supported by shale compaction and the great abundance of ice front features. Between 110,000 years ago and 20,000 years ago the ice sheet grows to its maximum extent. Subsequently it follows the relatively well documented retreat (Mangerud, 1979; Andersen, 1981; Lundqvist, 1986) illustrated in Fig. 7b. 9000 years ago the ice sheet has fully disappeared and we monitor the model until the present time.

The sediments in the northern North Sea are fairly unconsolidated to a depth of ≈1000 m. Unconsolidated sediments are incapable of supporting differential stress. Therefore, we expect that imposed bending stresses are only taken up by rock units at depths greater than 1000 m. As a result, the surface of the model corresponds to a real depth of ≈1000 m. Consequently, we shifted the modeled results with depth, e.g. 2000 m depth in Fig. 8 corresponds to 1000 m model depth.

The predicted present day stress perturbations along the profile line in the northern North Sea are displayed in Figs. 8a) and b). First, it is important to note that the numerical model predicts increased horizontal stresses in the western part of the northern North Sea, including the Tampen Spur and lowered horizontal stresses in proximity of the coast. This agrees well with the observed drop of horizontal stresses towards the coast (Fig. 2a) and also with the results of the analytical unloading model. But, for the numerical model we did not have to make any assumptions for the stress state before the onset of ice melting. Further, the entire upper crust is purely elastic and therefore can not relax deviatoric stresses at all.

Instead, the transition from lowered horizontal stresses in the proximity of the coast to higher horizontal stresses further offshore is the result of creep deformation that takes place in the lower crust during the ice sheet's existence. The lower crust and lithospheric

mantle horizontally extend underneath the ice sheet. As a result of the coupling between the lower and the upper crust, the lower crust transmits the horizontal extension to the upper crust which leads to the observed and modeled horizontal stress decrease in proximity of the coast at shallow depth. Away from the former ice sheet, a similar effect causes the present-day increase of the horizontal stresses. In other words, the ductile part of the lithosphere behaves similar to the end member model illustrated in Fig. 4a, while the upper crust follows the assumption made in Fig. 4b. The resulting modeled present-day stresses are comparable to what is expected from the assumption made in Fig. 4a but for a slightly different reason.

More specifically, compared to the analytical model, i.e. the assumption made in Fig. 4a, the amplitudes of the stress perturbations are smaller. The predicted S_1/S_v (Fig. 8a) is high on the west side of the Viking Graben and has a maximum value of 1.22 in the vicinity of the Visund field at relatively shallow depth. This matches the S_1/S_v estimates of Wiprut and Zoback (1998) for the Visund field very well (S_1/S_v between 1.2 and 1.3). Closer to the coast (i.e. east of the Viking Graben), S_1 is equal to S_v which would lead to a normal faulting stress regime. Predicted values for S_3/S_v (Fig. 8b) are close to 1 west of the Viking Graben and drop to minimum values of 0.88 in the region of block 35/9. The lateral extent of the predicted changes in horizontal stress match the measured stresses, with maxima in the Tampen Spur and minima in proximity of block 35/9.

Fig. 8c compares the modeled uplift rates with estimates obtained from mareograph and precise leveling data (Ekman, 1996) from the coast towards the center of the ice sheet. The model achieves a good fit to the uplift measurements. Except in proximity to the coast where the modeled uplift rates fall slightly outside the error bounds of the measurement. A possible reason for this discrepancy is the two-dimensional geometry of the model which implies that the ice sheet front was always oriented perpendicular to the modeled cross section. Fig. 1 shows that this is not the case for the maximum ice sheet extent.

We also considered an ice model that consists of ten ice loading cycles with a

periodicity of 10^5 years based on oxygen isotope curves obtained from deep sea drilling (Shackleton et al., 1984). Otherwise the model is identical to the single loading cycle-model described above. Compared to the model with a single loading cycle (Fig. 8) the horizontal stress perturbations are lower. S_1/S_v reaches a maximum of 1.1 and S_3/S_v varies between 1 and 0.91 (Fig. 9, a and b). Even if the magnitudes of the stress perturbation are lower than in the single loading cycle-model the general pattern of the stress perturbations is identical with high horizontal stresses (i.e. strike-slip/thrust faulting) west of the Viking Graben and lower horizontal stresses (i.e. strike-slip/normal faulting) between the Viking Graben and the coast. The predicted uplift rates (Fig. 9c) are almost identical for both models.

In both numerical models, the zone of decreased horizontal stress beneath the former ice sheet is limited to within 100-150 km of the ice sheet front. Closer to the center of the ice sheet the modeled horizontal stress perturbations diminish. As mentioned earlier, the stress state obtained from earthquakes and postglacial fault movements is predominantly thrust faulting near the center of the ice sheet which is compatible with the model results. The induced stress perturbations decrease with depth, which is a typical feature for bending stresses. However, the predicted horizontal stresses are slightly to low. A possible explanation for this underprediction of horizontal stress is the fact that we ignore ridge push as a stress source. As mentioned earlier, ridge push uniformly increases horizontal stress over large areas.

Also, note that the modeled upper crust has a purely elastic rheology, lacking the possibility to undergo brittle deformation. We chose the purely elastic rheology because we wanted to keep the model as simple as possible without complicating it unnecessarily. The fact that we can model the observed stresses without accounting for brittle failure indicates that the observed in-situ stress variations are mostly the result of the previously described interaction between the ductile lower crust and the strong, elastic upper crust.

4. Prediction of pore pressure from glacial unloading

Comparing Fig. 2a and Fig. 2b it is evident that the pore pressure is somehow related to stress. The highest pore pressures occur in the Tampen Spur, where S_3/S_v is close to 1, indicating high horizontal stresses. Conversely, east of the Viking Graben the pore pressure is mostly hydrostatic and S_3/S_v drops to ≈0.8 in the same region. In the previous sections we have established that the increased horizontal stresses in the Tampen Spur are likely to be caused by glaciation-deglaciation and therefore developed very recently (since 20,000 years ago). So, perhaps part of the overpressure in the Tampen Spur results from the poroelastic response to the stress increase that was induced by deglaciation.

To test this hypothesis, we calculated the change in the modeled 1st stress invariant ($\Delta\sigma_m$) between the onset of the model and present, which corresponds to the change of the isotropic part of the stress tensor and is a measure for the volume change a certain rock mass was exposed to. $\Delta\sigma_m$ is related to a change in pore pressure (ΔP_p), via Skempton's coefficient (B), where B varies between 0 and 1. For B=1 the change in P_p is equal to $\Delta\sigma_m$ and for B=0 any change in $\Delta\sigma_m$ doesn't affect the pore pressure.

Fig. 10 shows the predicted ΔP_p as a result of glaciation-deglaciation for B=0.8, which is an upper bound for realistic values of B and typical for shales. Reservoir sands with high porosities typically have B-values of ≈0.5. We chose a relatively high B-value since we wanted to get an upper bound on how deglaciation influences the pore pressure.

The highest modeled ΔP_p of 3.5 MPa occurs where the horizontal stress increases the most, which is west of the Viking Graben in the vicinity of the Snorre and Visund fields. In the Snorre field ΔP_p is predicted to be around 3.5 MPa and in Visund it drops to 2.8 MPa. Closer to the coast, e.g. in block 35/9 ΔP_p is negative so we would actually expect a P_p decrease, leading to subhydrostatic pore pressures in proximity of the coast. If we compare these P_p predictions to the observed P_p-values shown in Fig. 2b, it becomes obvious that the predicted P_p-increase in Snorre (3.5 MPa) and Visund (2.8 MPa) are much smaller than measured overpressures, which reach up to 15 MPa in the Tampen Spur.

Conversely, we don't observe subhydrostatic pore pressures around block 35/9 as predicted by the model.

A possible explanation for the higher than predicted pore pressures in the Tampen Spur are additional sources of overpressure, such as under-compaction. If the overburden due to sedimentation increases faster than pore fluids can diffuse away the pore pressure increases. Caillet et al. (1991) modeled P_p-increases resulting from this effect for the Tampen Spur. For Visund they predict overpressures of around 7 MPa at 2500 m depth and 12 MPa for a depth of 3000 m. However, measured pore pressures are typically around 5 MPa higher. After adding the overpressure of 2.8 MPa due to deglaciation to the under-compaction prediction, we actually get closer to the observed pore pressures. The same applies to the Snorre field where the combined overpressure from under-compaction and deglaciation gets very close to the observed pore pressures. Therefore, the overpressures in the Tampen Spur seem to be the result of both, under-compaction and poroelastic response to bending stresses induced by glaciation-deglaciation.

Concerning the predicted P_p-decrease close to the coast, we have to take into account that in this area stresses are strongly decreased which tends to cause faulting, and consequently increases permeability (e.g. Barton et al., 1995). As a result of increased permeability the pore fluids communicate with the sea floor and no subhydrostatic pore pressure can develop.

An alternative explanation for the low P_p close to the coast is the stress decrease that deglaciation induced. The P_p can never exceed S_3 since this would lead to fracturing of the formation and as a result the fluids would escape to the surface. The stress decrease due to deglaciation might have brought S_3 down to the existing pore pressure at the time when the stress decrease took place and parts of the fluids leaked away, leading to a P_p reduction. Possibly, the expected P_p decrease due to poroelasticity from Fig. 10 was superimposed onto this effect, leading to the close to hydrostatic pore pressures at present. Conversely, in the Tampen Spur where stresses remained high, the high overpressures

were contained.

5. Conclusions

Observed stress data in the northern North Sea shows a transition from high horizontal stresses in the Tampen Spur to decreased stresses towards the coast. Modeling of flexural stresses due to glaciation-deglaciation shows that this lateral stress variation is likely to be the result of this process. The regionally consistent orientation of S_{Hmax} as well as the underprediction of stress magnitudes by the flexural models suggests that ridge push also significantly contributes to the stress state in the northern North Sea. The wavelength of the stress perturbation implies that the effective elastic lithospheric thickness in the northern North Sea ranges between 30 and 40 km on a timescale comparable to deglaciation (≈10,000 years).

Concerning the model it shouldn't be forgotten that we limited ourselves to a two-dimensional approach which has the advantage of simplicity. However, by doing so we have to assume that the changes in ice sheet thickness are largest parallel to the modeled cross section. Fig. 1 shows that this is not true for the maximum ice sheet extent 20,000 years ago. Nevertheless, the modeling shows that deglaciation is a possible source of overpressure in the Tampen Spur. However, part of the observed overpressure must have been caused by another source such as compaction disequilibrium resulting from rapid sedimentation.

Acknowledgments

We would like to thank Norsk Hydro for generously providing the data and financial support for this study.

Appendix A. Analytical model of viscoelastic bending of the lithosphere under distributed pressure

According to Nadai (1963), if the lithosphere is a "Maxwell" viscoelastic layer with thickness T underlain by a fluid substratum accounting for isostasy the time dependent flexural deflection $w_{(x,t)}$ as a result of a distributed load $P_{(x,t)}$ can be described with the following equation:

$$D\frac{\partial^4}{\partial x}(w') = -k\left(w' + \frac{w}{\tau}\right) + P' + \frac{P}{\tau} \qquad (A1)$$

where the flexural rigidity is $D=ET^3/9$ for $\nu=0.5$, τ is the relaxation time, $k = g(\rho_a-\rho_w)$ is the density restoring force if the lithosphere is covered by water. In case of a dry surface $k = g\rho_a$. w' and P' are the time differentiations of w and P.

The solution to A1 for a periodic load is

$$w(x, t) = \frac{P_0}{k}\sum_{n=1}^{\infty}\varphi_n(t)C_n\cos\frac{n\pi x}{a} \qquad (A2)$$

If the load has a constant thickness h_{ice} a half width c and the load edge is located at distance a from the origin (x=0) then

$$C_n = \frac{-1^n}{n}\sin\frac{n\pi c}{a} \qquad (A3)$$

and

$$P_0 = \frac{2}{\pi}\rho_{ice}h_{ice}g \qquad (A4)$$

and φ_n for an exponentially growing load

$$\varphi_n(t) = \frac{\left\{(t_p-\tau)\left(1-e^{-\frac{t}{t_p}}\right)-(t_n-\tau)\left(1-e^{-\frac{t}{t_n}}\right)\right\}}{t_p-t_n} \qquad (A5)$$

t_n is the characteristic time for each Fourier term

$$t_n = \left\{1 + \left(\frac{D}{k}\right)\left(\frac{n\pi}{a}\right)^4\right\}\tau \qquad \text{(A6)}$$

and t_p determines how fast the load is applied. Values much smaller than unity correspond to an instantaneous growth. The flexural stress can be calculated with

$$S_{xx}(x, z, t) = \frac{4EzP_0}{3k}\sum_{n=1}^{\infty}\left(\frac{n\pi}{a}\right)^2 f_n(t)C_n\cos\frac{n\pi x}{a} \qquad \text{(A7)}$$

where z is depth and

$$f_n(t) = \frac{\tau}{(t_p - t_n)\left(e^{-\frac{1}{t_p}} - e^{-\frac{t}{t_n}}\right)} \qquad \text{(A8)}$$

Because the applied load is periodic, i.e. another ice sheet exists at x=-a, the solutions are governed by the boundary condition dw/dx = 0 at x=0.

Appendix B.

List of symbols

S_{Hmax}	Maximum horizontal stress, [MPa]
S_1	Maximum principal stress, [MPa]
S_3	Least principal stress, [MPa]
S_v	Vertical stress, [MPa]
P_p	Pore pressure, [MPa]
T	Effective elastic thickness of the lithosphere, [m]
h_{ice}	Thickness of the ice sheet, [m]
c	Half width of the ice sheet, [m]
a	Distance of ice edge from x=0, [m]
τ	Maxwell relaxation time, [a]
ρ	Density, [kg/m^3]
ρ_a	Asthenospheric density, [kg/m^3]

ρ_{ice}	Density of ice, [kg/m^3]
ρ_w	Density of water, [kg/m^3]
E	Young's modulus, [GPa]
ν	Poisson's ratio
η	Viscosity, [Pa s]
σ_m	First stress invariant ($1/3\sigma_{ii}$), [MPa]
B	Skempton's coefficient ($P_p/\Delta\sigma_m$)

References

Andersen, B.G., 1981. Late Weichselian Ice Sheets in Eurasia and Greenland. In: Denton, G.H., Hughes, T.J. (Eds.), The Last Great Ice Sheets. Wiley, New York, pp. 1-65.

Anderson, E.M., 1951. The Dynamics of Faulting and Dyke Formation with Applications to Britain. Oliver and Boyd, Edinburgh.

Barton, C.A., Zoback, M.D., Moos, D., 1995. Fluid flow along potentially active faults in crystalline rock. Geology 23(8), 683-686.

Bott, M.H.P., Kusznir, N., 1984. The origin of tectonic stress in the lithosphere. Tectonophysics 105, 1-13.

Bungum, H., 1989. Earthquake occurrence and seismotectonics in Norway and surrounding areas. In: Gregersen, S., Basham, P.W. (Eds.), Earthquakes at North-Atlantic Passive Margins: Neotectonics and Postglacial Rebound. Kluwer Academic Publishers, Dordrecht, pp. 501-519.

Caillet, G., Sejourne, C., Grauls, D., Arnaud, J., 1991. The hydrodynamics of the Snorre Field area, offshore Norway. Terra Nova 3, 180-194.

Denton, G.H., Hughes, T., 1981. The last great ice sheets. John Wiley and Sons, New York.

Dore, A.G., 1992. The base Tertiary surface of southern Norway and the northern North Sea. Norsk Geologisk Tidsskrift 72, 259-265.

Dragoni, M., Pasquale, V., Verdoya, M., Chiozzi, P., 1993. Rheological consequences of the lithospheric thermal structure in the Fennoscandian Shield. Global and Planetary Change 8, 113-126.

Ekman, M, 1996. A consistent map of the postglacial uplift of Fennoscandia. Terra Nova 8, 158-165.

Ekman, M., Makinen, J., 1996. Recent postglacial rebound, gravity change and mantle flow in Fennoscandia. Geophys. J. Int. 126, 229-234.

Fjeldskaar, W., 1997. Flexural rigidity of Fennoscandia inferred from the postglacial uplift. Tectonics 16(4), 596-608.

Forsyth, D., Uyeda, S., 1975. On the relative importance of the driving forces of plate motion. Geophys. J. R. Astr. Soc. 43, 163-200.

Goelke, M., 1996. Patterns of stress in sedimentary basins and the dynamics of pull-apart basin formation. Ph.D. Thesis, Vrije Universiteit. Amsterdam, Netherlands.

Gregersen, S., Korhonen, H., Husebye, E.S., 1991. Fennoscandian dynamics: Present-day earthquake activity. Tectonophysics 189, 333-344.

Grollimund, B., Zoback, M.D., Wiprut, D.J., Arnesen, L., in press. Regional synthesis of stress orientation, pore pressure and least principle stress data in the Norwegian sector of the North Sea. Petroleum Geoscience.

Hansen, S., 1996. Quantification of net uplift and erosion on the Norwegian Shelf south of 66°N from sonic transit times of shale. Norsk Geologisk Tidsskrift 76, 245-252.

Jaeger, J.C., Cook, N.G.W., 1979. Fundamentals of Rock Mechanics. Chapman and Hall, London.

James, T.S., Bent, A.L., 1994. A comparison of eastern North American seismic strain-rates to glacial rebound strain-rates. Geophys. Res. Lett. 21, 2127-2130.

Johnston, P., Wu, P., Lambeck, K., 1998. Dependence of horizontal stress magnitude on load dimension in glacial rebound models. Geophys. J. Int. 132, 41-60.

Klemann, V., Wolf, D., 1998. Modelling of stresses in the Fennoscandian lithosphere induced by Pleistocene glaciations. Tectonophysics 294, 291-303.

Lindholm, C.D., Bungum, H., Villagram, M., Hicks, E., 1995. Crustal Stress and Tectonics in Norwegian Regions Determined from Earthquake Focal Mechanisms. Proc. Workshop on Rock Stresses in the North Sea, Trondheim, Norway, pp. 77-91.

Lundqvist, J., 1986. Late Weichselian glaciation and deglaciation in Scandinavia. Quaternary Science Reviews 5, 269-292.

Mangerud, J., Larsen, E., Longva, O., Sonstegaard, E., 1979. Glacial History of Western Norway 15,000-10,000 B.P. Boreas 8, 2, 179-187.

Muir Wood, R., 1989. Extraordinary deglaciation reverse faulting in northern

Fennoscandia. In: Gregersen, S., Basham, P.W. (Eds.), Earthquakes at North-Atlantic Passive Margins: Neotectonics and Postglacial Rebound. Kluwer Academic Publishers, Dordrecht, pp. 141-173.

Müller, B., Zoback, M.L., Fuchs, K., Mastin, L., Gregersen, S., Pavoni, N., Stephansson, O., Ljunggren, C., 1992. Regional Patterns of Tectonic Stress in Europe. J. Geophys. Res. 97:B8, 11783-11803.

Nadai, A., 1963. Theory of Flow and Fracture of Solids. McGraw-Hill, New York.

Parsons, B., Richter, F.M., 1980. A relation between the driving force and geoid anomaly associated with mid-ocean ridges. Earth and Planetary Science Letters 51(2), 445-450.

Peltier, W.R., 1976. Glacial-isostatic adjustment-II. The inverse problem. Geophys. J. R. astr. Soc. 46, 669-705.

Shackleton, N.J., Backman, J., Zimmerman, H., Kent, D.V., Hall, M.A., Roberts, D.G., Schnitker, D., Baldauf, J.G., Desprairies, A., Homrighausen, R., Huddlestun, P., Keene, J.B., Kaltenback, A.J., Krumsiek, K.A.O., Morton, A.C., Murray, J.W., Westberg-Smith, J., 1984. Oxygen isotope calibration of the onset of ice-rafting and history of glaciation in the North Atlantic region. Nature 307, 620-623.

Stein, S., Cloetingh, S., Sleep, N.H., Wortel, R., 1989. Passive Margin Earthquakes, Stresses and Rheology. In: Gregersen, S., Basham, P.W. (Eds.), Earthquakes at North-Atlantic Passive Margins: Neotectonics and Postglacial Rebound. Kluwer Academic Publishers, Dordrecht, pp. 231-259.

Stephansson, O., 1988. Ridge push and glacial rebound as rock stress generators in Fennoscandia. Bull. Geol. Inst. Univ. Uppsala 14, 39-48.

Strehlau, J., Meissner, R., 1987. Estimation of crustal viscosities and shear stresses from an extrapolation of experimental steady state flow data. In: Fuchs, K., Froidevaux C. (Eds.), Composition, Structure and Dynamics of the Lithosphere-Asthenosphere System. AGU, GSA, pp. 69-87.

Walcott, R.I., 1970. Isostatic response to loading of the crust in Canada. Can. J. Earth. Sci.

7, 716-727.

Wiprut, D.J., Zoback, M.D., 1998. High horizontal stress in the Visund field, Norwegian North Sea. Proc. Eurock, Trondheim, Norway. SPE, pp. 199-208.

Wolf, D., 1987. An upper bound on lithospheric thickness from glacio-isostatic adjustment in Fennoscandia. J. Geophys. 61(3), 141-149.

Wu, P., 1997. Effects of viscosity structure on fault potential and stress orientations in eastern Canada. Geophys. J. Int. 130, 365-382.

Zoback, M.L., 1992. First- and Second-Order Patterns of Stress in the Lithosphere: The World Stress Map Project. J. Geophys. Res. 97:B8, 11703-11728.

Table 1: Parameters used in the numerical model

	ρ [kg/m^3]	E [GPa]	ν	η [Pa s]	thickness [km]
Sediments	2350	56	0.25	-	5
Upper crust	2700	56	0.25	-	15
Lower crust	2900	71	0.25	10^{22}	15
Upper mantle	3200	100	0.25	10^{23}	15
Asthenosphere	3300	-	-	$3x10^{19}$	-

Figure Captions

Figure 1: Overview map.of western Norway and the northern North Sea. The bold lines show S_{Hmax} orientations inferred from drilling induced tensile fractures (Wiprut and Zoback, 1998) and the narrow black lines illustrate S_{Hmax} orientations from borehole breakouts. S_{Hmax} rotates from ≈100° west of the Viking Graben to ≈80° closer to the coast. The circles, squares and diamonds show locations of earthquakes with their respective faulting regime. The dashed lines are isolines of ice sheet thickness for the maximum extent 20,000 years ago from Andersen (1981). The light grey areas illustrate the lateral extents of known hydrocarbon fields.

Figure 2: Observed stress and pore pressure in the northern North Sea. In Fig. 2a the colored surface shows spatial variations of S_3 as inferred from leak-off test, normalized by S_v from integrated density logs. S_3/S_v is close to 1 in the fields of the Tampen Spur (Snorre, Visund) but decreases towards the coast. The maximum decrease occurs at a depth of 2500 m. The blue asterisks show S_{Hmax}/S_v and are obtained from the analysis of the full stress tensor from wellbore failure in Visund (Wiprut and Zoback, 1998) and suggest a strike-slip to almost reverse faulting stress state in the Visund field. In Fig. 2b the colored surface shows spatial variations of P_p mostly from RFT-logs and from drill stem tests, normalized by S_v from integrated density logs.The plot shows that in Snorre and Visund formations are severely overpressured at depths greater than 1500 m. Closer to the coast, P_p is close to hydrostatic down to 3000 m.

Figure 3: Map view of stress and pore pressure in the North Sea. Fig. 3a shows the least principal stress normalized by the overburden (S_3/S_v) for a depth of 2500 m. The figure shows that S_3/S_v is consistently low close to the coast and increases towards the west (perpendicular to the coast line). Fig. 3b shows the pore pressure normalized by the overburden (P_p/S_v) at a depth of 2500 m. The pore pressure is mostly hydrostatic but

highly overpressured west of the Viking Graben (Tampen Spur). Slight overpressure also occurs in the southern North Sea.

Figure 4: Illustration about how flexural stresses affect the stress field. Fig. 4a assumes that bending stresses relax during the existence of the ice sheet. Subsequent melting leads to extension under the former ice sheet and compression further offshore with increasing amplitude as the rebound goes on. In the case of Fig. 4b it is assumed that relaxation processes are insignificant during the duration of glaciation. After ice melting stresses are still compressive under the former ice sheet and extensive further offshore but decrease as the rebound goes on.

Figure 5: Viscoelastic model for flexural stresses as a result of ice loading. The lithosphere is modeled as a viscoelastic layer underlain by a fluid substratum. The model assumes loading of the lithosphere for 2 Ma by an ice sheet with 1 km thickness. The upper graph for each subplot shows expected bending stresses at the surface for different time slices with an increment size of 200,000 years (decreasing magnitude with time). The lower graph illustrates the bending stresses as a function of depth predicted for 2 Ma after the onset of ice loading. Compressive stresses are positive.

Figure 6: Elastic model for flexural stresses as a result of ice melting. The lithosphere is modeled as an elastic layer underlain by a fluid substratum. The model assumes that no bending stresses existed before the ice sheet started to melt. The upper graph shows predicted present day bending stresses at the surface for different effective elastic thicknesses of the lithosphere (T). The lower graph illustrates bending stresses as a function of depth for T=30 km. Compressive stresses are positive.

Figure 7: Setup of the numerical model and assumed ice sheet history. Fig. 7a shows the rheologies of the model. The upper crust is elastic and divided into sediments and basement. The basement has a higher density than the sediments. The lower crust and the

upper mantle are assumed to be Maxwell-viscoelastic to account for time-dependent irreversible deformation. The asthenosphere is modeled as a viscous semi-infinite substratum. Fig. 7b shows the modeled ice sheet geometry. The ice sheet grows 1.1 Ma years ago and has a constant extent until 110,000 years ago. Then it grows to its maximum extent (20,000 years ago) and subsequently melts. The ice sheet is assumed to be melted entirely 9000 years ago.

Figure 8: Predicted stress from numerical model with a single loading-cycle. The colored surfaces show the predicted spatial variations of S_1/S_v and S_3/S_v for the present. The observed stress decrease towards the coast is reproduced by the model. However, west of the Viking Graben the model underpredicts the observed stresses, which suggests that ridge push also contributes to the horizontal stresses. Fig. 8c compares the modeled uplift rate to estimates from mareograph and precision leveling data.

Figure 9: Predicted stress from numerical model with multiple loading-cycles. The colored surfaces show the predicted spatial variations of S_1/S_v and S_3/S_v for the present. The observed stress decrease towards the coast is reproduced by the model. Compared to the single loading cycle model stress perturbations are smaller but show the same patterns. Fig. 9c compares the modeled uplift rate to estimates from mareograph and precision leveling data.

Figure 10: Predicted pore pressure change from glaciation-deglaciation. The figure shows the potential for a change in pore pressure as a result of poroelastic response to deglaciation for B=0.8. The predicted pore pressure increase is highest in the vicinity of the Snorre field with increases of 3.5 MPa. Closer to the coast, P_p remains almost constant or slightly decreases.

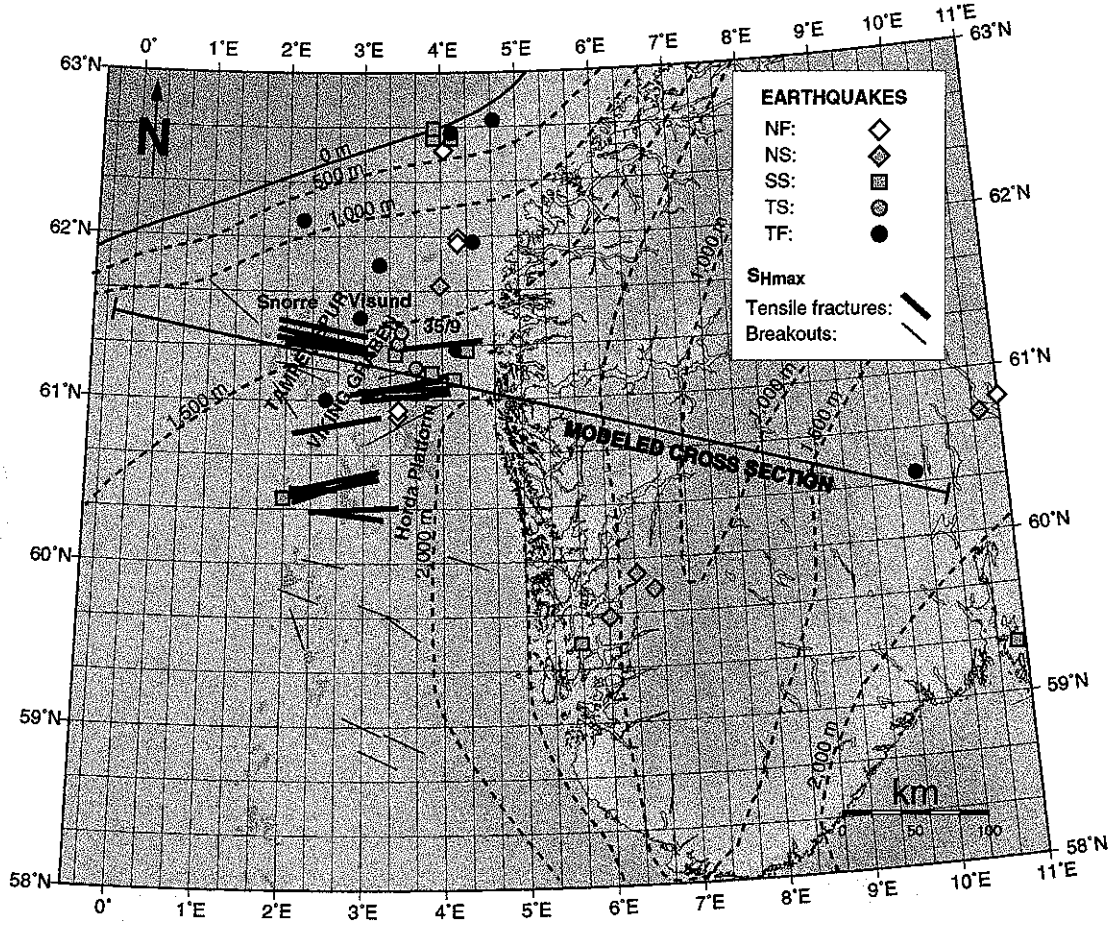
EARTHQUAKES
NF:
NS:
SS:
TS:
TF:
S_{Hmax}
Tensile fractures:
Breakouts:
MODELED CROSS SECTION
Snorre
Visund
Horda Platform
km
0
50
100
63°N
62°N
61°N
60°N
59°N
58°N
0°
1°E
2°E
3°E
4°E
5°E
6°E
7°E
8°E
9°E
10°E
11°E

Figure 1

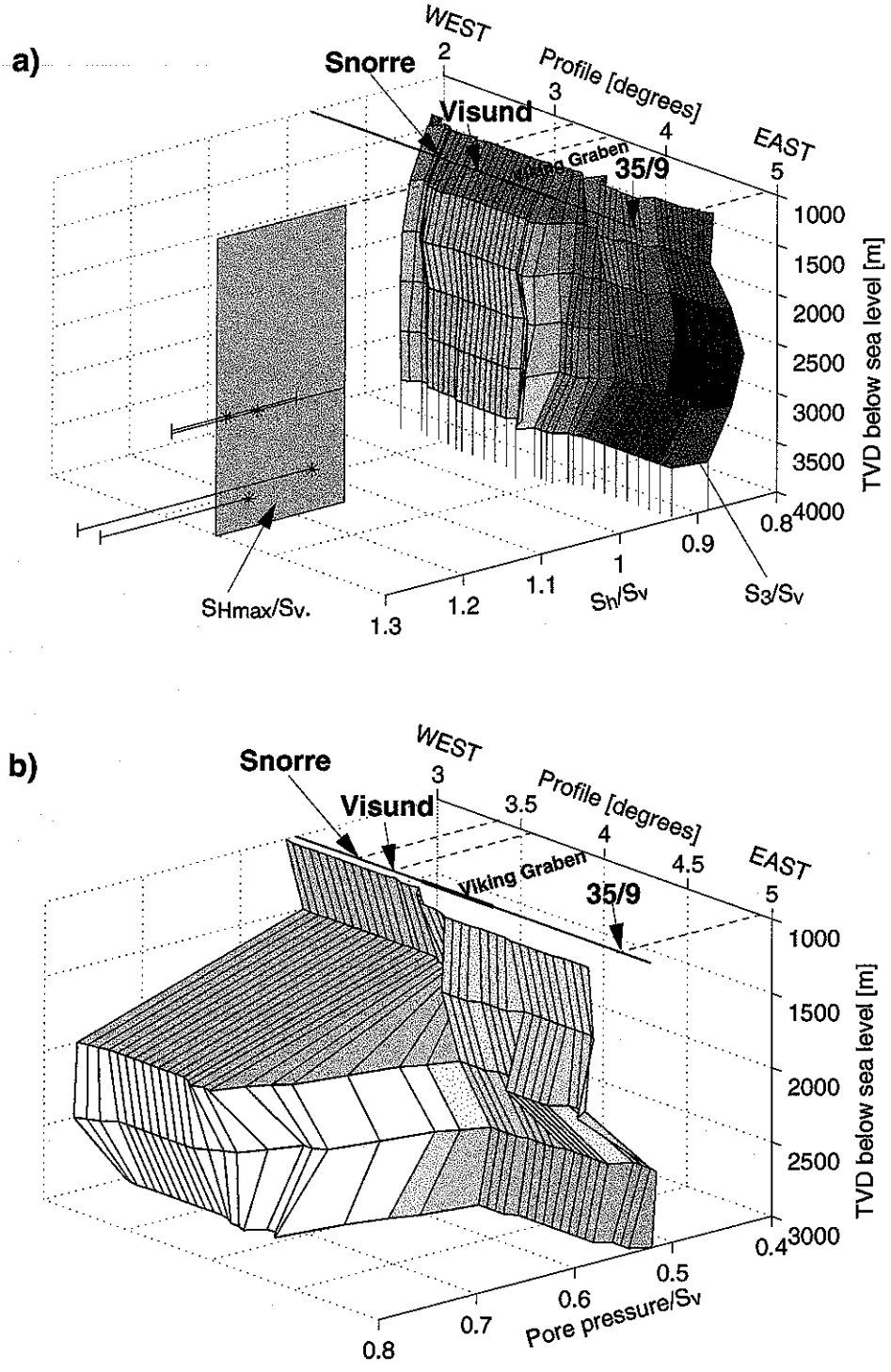
a)
WEST
Snorre
Visund
Profile [degrees]
EAST
Viking Graben
35/9
TVD below sea level [m]
SHmax/Sv.
Sh/Sv
S3/Sv
b)
WEST
Snorre
Visund
Profile [degrees]
EAST
Viking Graben
35/9
TVD below sea level [m]
Pore pressure/Sv

Figure 2

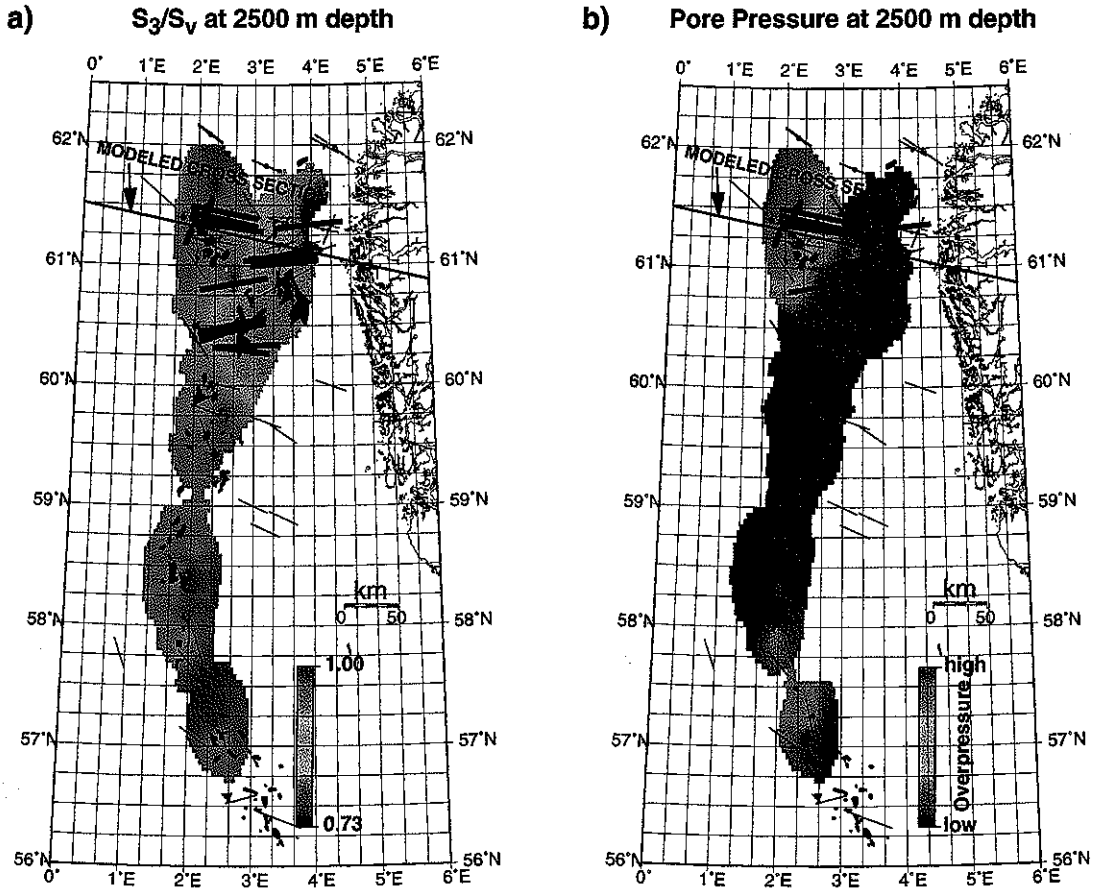
a)
S_3/S_V at 2500 m depth
b)
Pore Pressure at 2500 m depth
MODELED CROSS SEC
km
0 50
1.00
0.73
high
Overpressure
low
0°
1°E
2°E
3°E
4°E
5°E
6°E
62°N
61°N
60°N
59°N
58°N
57°N
56°N

Figure 3

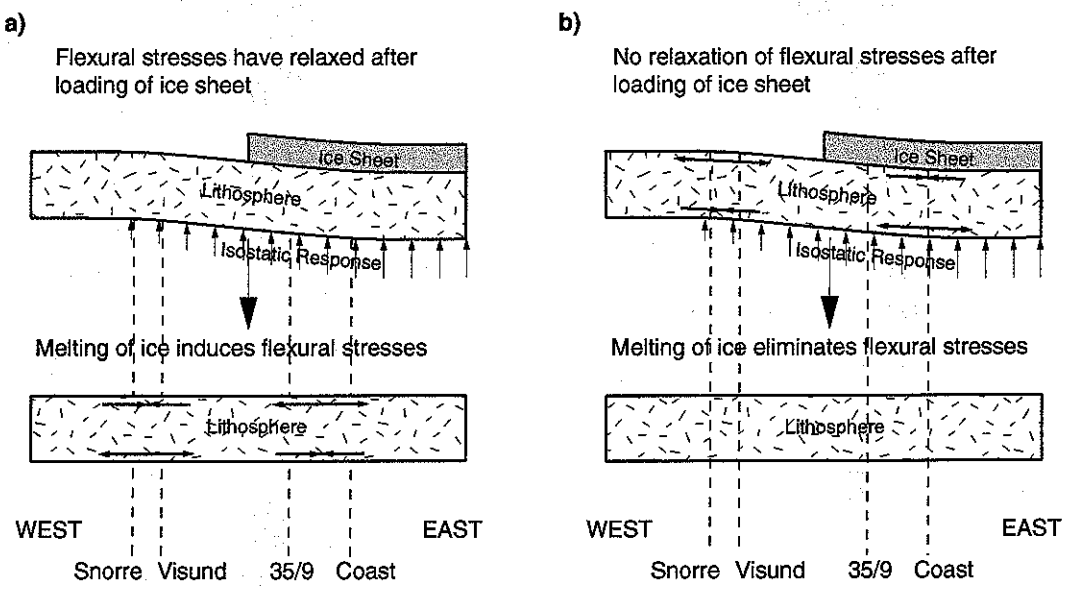
a)
Flexural stresses have relaxed after loading of ice sheet
Ice Sheet
Lithosphere
Isostatic Response
Melting of ice induces flexural stresses
Lithosphere
WEST
EAST
Snorre
Visund
35/9
Coast
b)
No relaxation of flexural stresses after loading of ice sheet
Ice Sheet
Lithosphere
Isostatic Response
Melting of ice eliminates flexural stresses
Lithosphere
WEST
EAST
Snorre
Visund
35/9
Coast

Figure 4

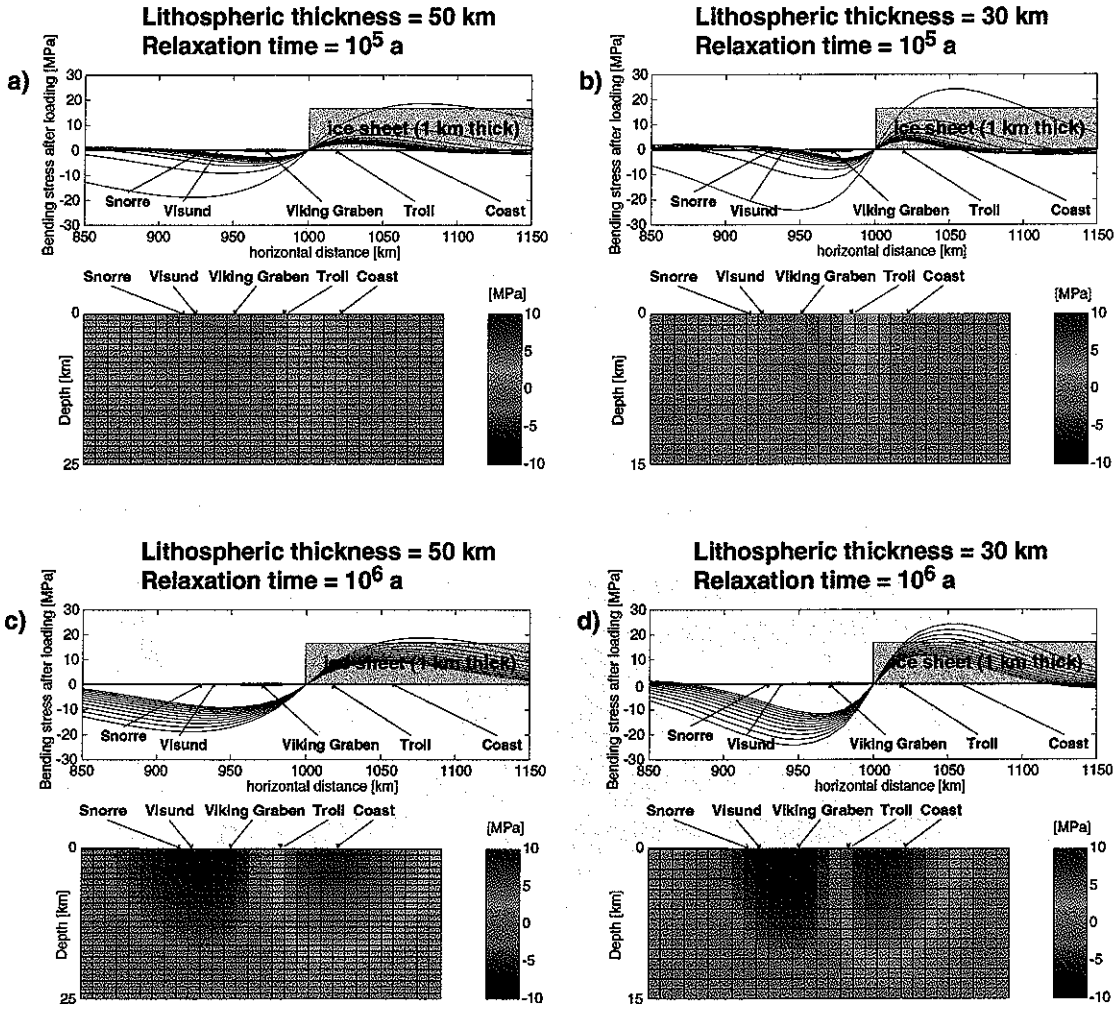
a)
Lithospheric thickness = 50 km
Relaxation time = 10^5 a
b)
Lithospheric thickness = 30 km
Relaxation time = 10^5 a
c)
Lithospheric thickness = 50 km
Relaxation time = 10^6 a
d)
Lithospheric thickness = 30 km
Relaxation time = 10^6 a
Bending stress after loading [MPa]
horizontal distance [km]
ice sheet (1 km thick)
Snorre
Visund
Viking Graben
Troll
Coast
Depth [km]
[MPa]

Figure 5

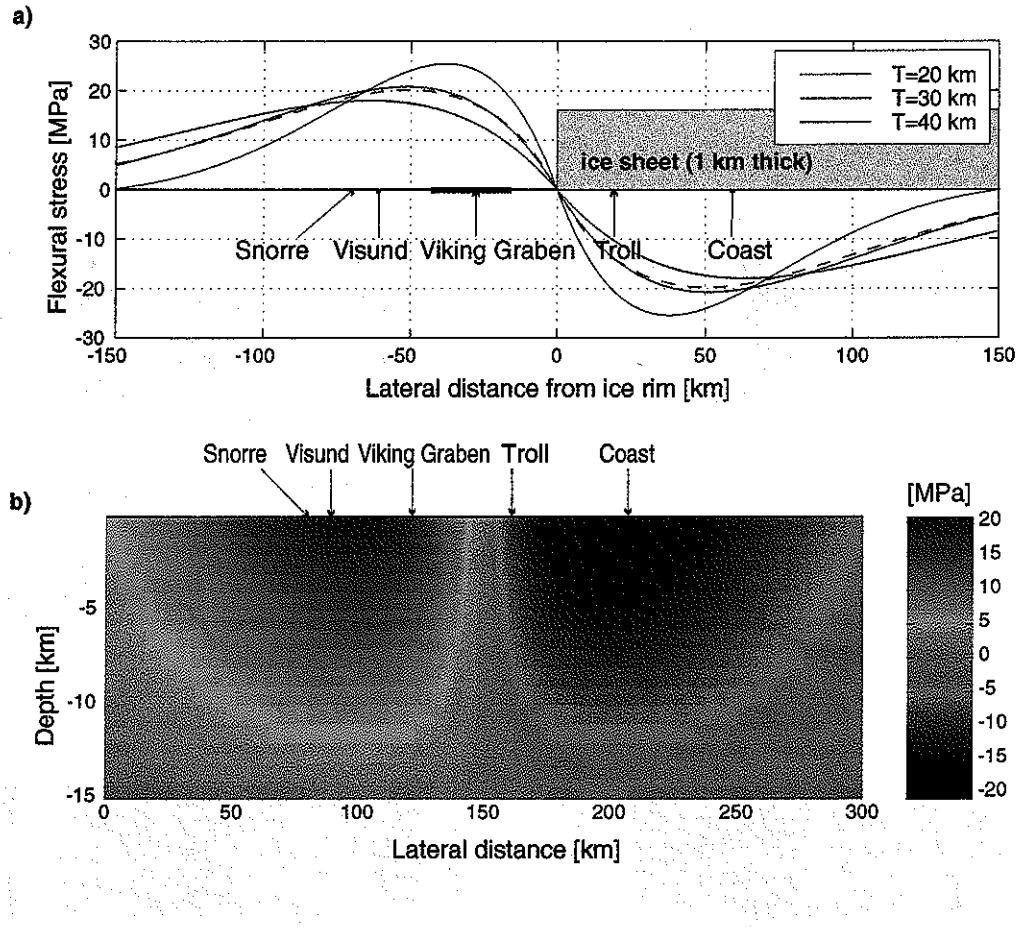
a)
Flexural stress [MPa]
30
20
10
0
-10
-20
-30
-150
-100
-50
0
50
100
150
T=20 km
T=30 km
T=40 km
ice sheet (1 km thick)
Snorre
Visund
Viking Graben
Troll
Coast
Lateral distance from ice rim [km]
b)
Snorre
Visund
Viking Graben
Troll
Coast
Depth [km]
-5
-10
-15
0
50
100
150
200
250
300
Lateral distance [km]
[MPa]
20
15
10
5
0
-5
-10
-15
-20

Figure 6

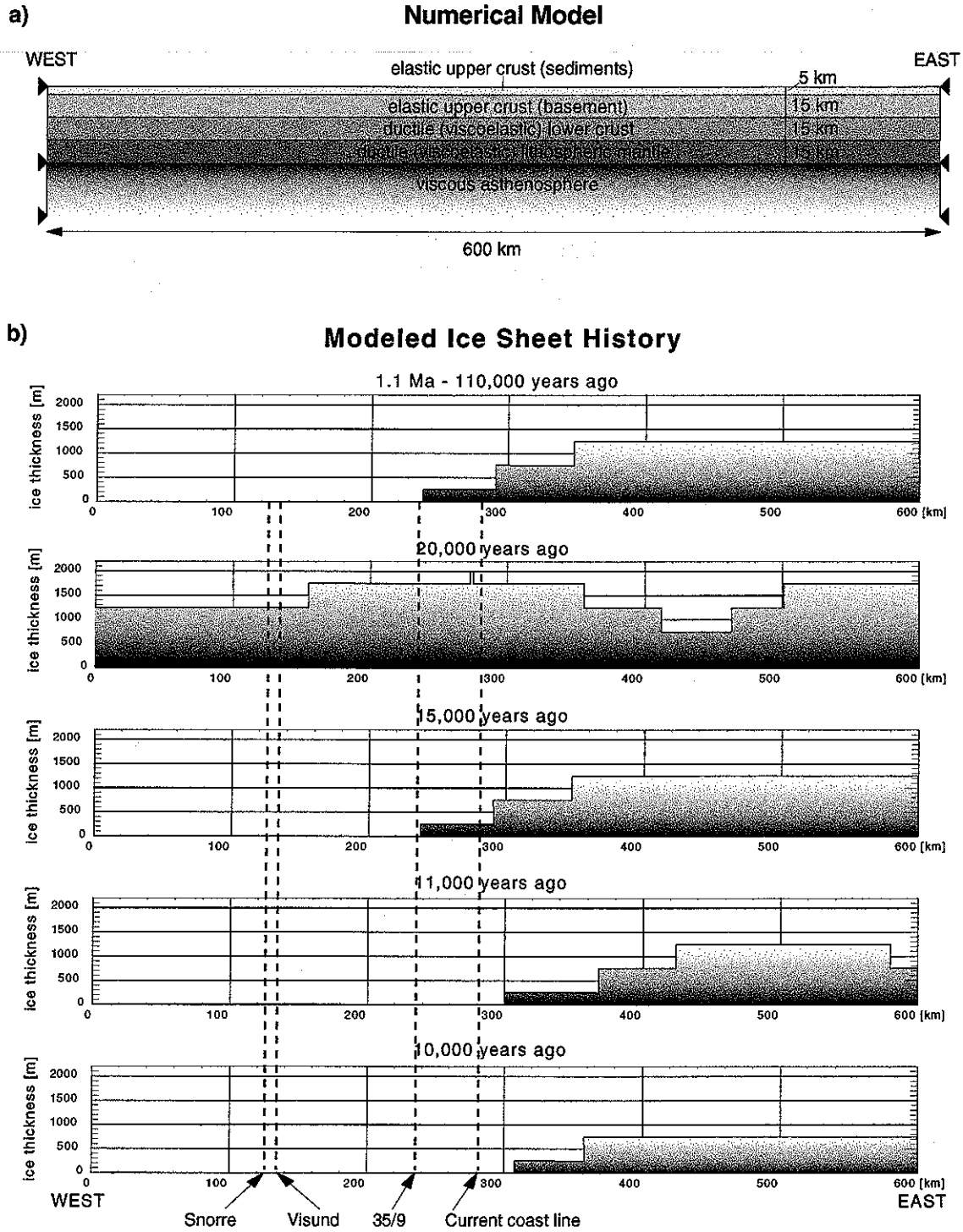
a)
Numerical Model
WEST
EAST
elastic upper crust (sediments)
5 km
elastic upper crust (basement)
15 km
ductile (viscoelastic) lower crust
15 km
ductile (viscoelastic) lithospheric mantle
15 km
viscous asthenosphere
600 km
b)
Modeled Ice Sheet History
1.1 Ma - 110,000 years ago
20,000 years ago
15,000 years ago
11,000 years ago
10,000 years ago
ice thickness [m]
2000
1500
1000
500
0
100
200
300
400
500
600 [km]
WEST
EAST
Snorre
Visund
35/9
Current coast line

Figure 7

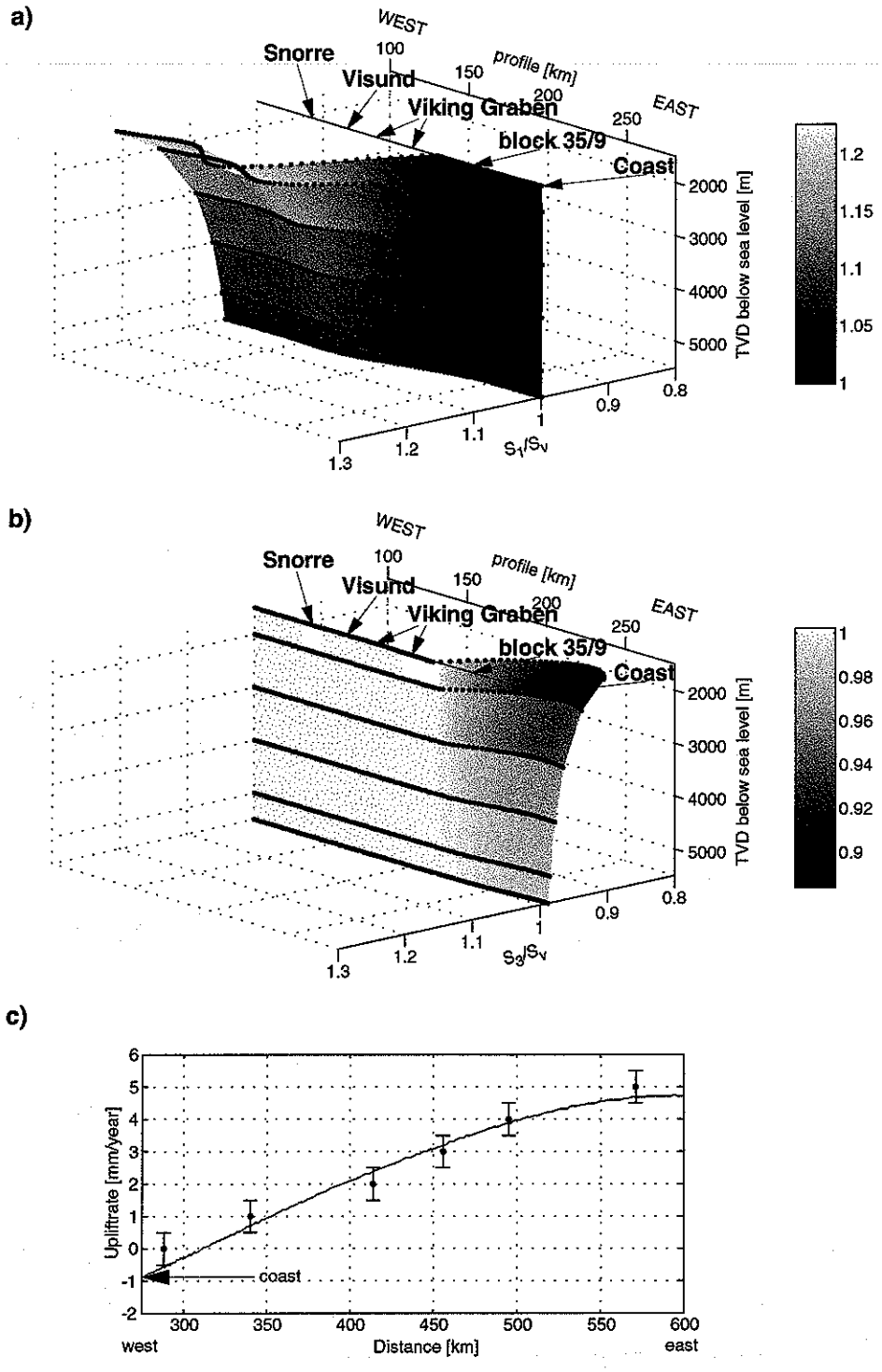
a)
WEST
Snorre
Visund
Viking Graben
block 35/9
Coast
EAST
profile [km]
100
150
200
250
2000
3000
4000
5000
TVD below sea level [m]
1.2
1.15
1.1
1.05
1
0.9
0.8
1.3
1.2
1.1
1
S1/Sv
b)
WEST
Snorre
Visund
Viking Graben
block 35/9
Coast
EAST
profile [km]
1
0.98
0.96
0.94
0.92
0.9
S3/Sv
c)
Uplift rate [mm/year]
coast
west
Distance [km]
east

Figure 8

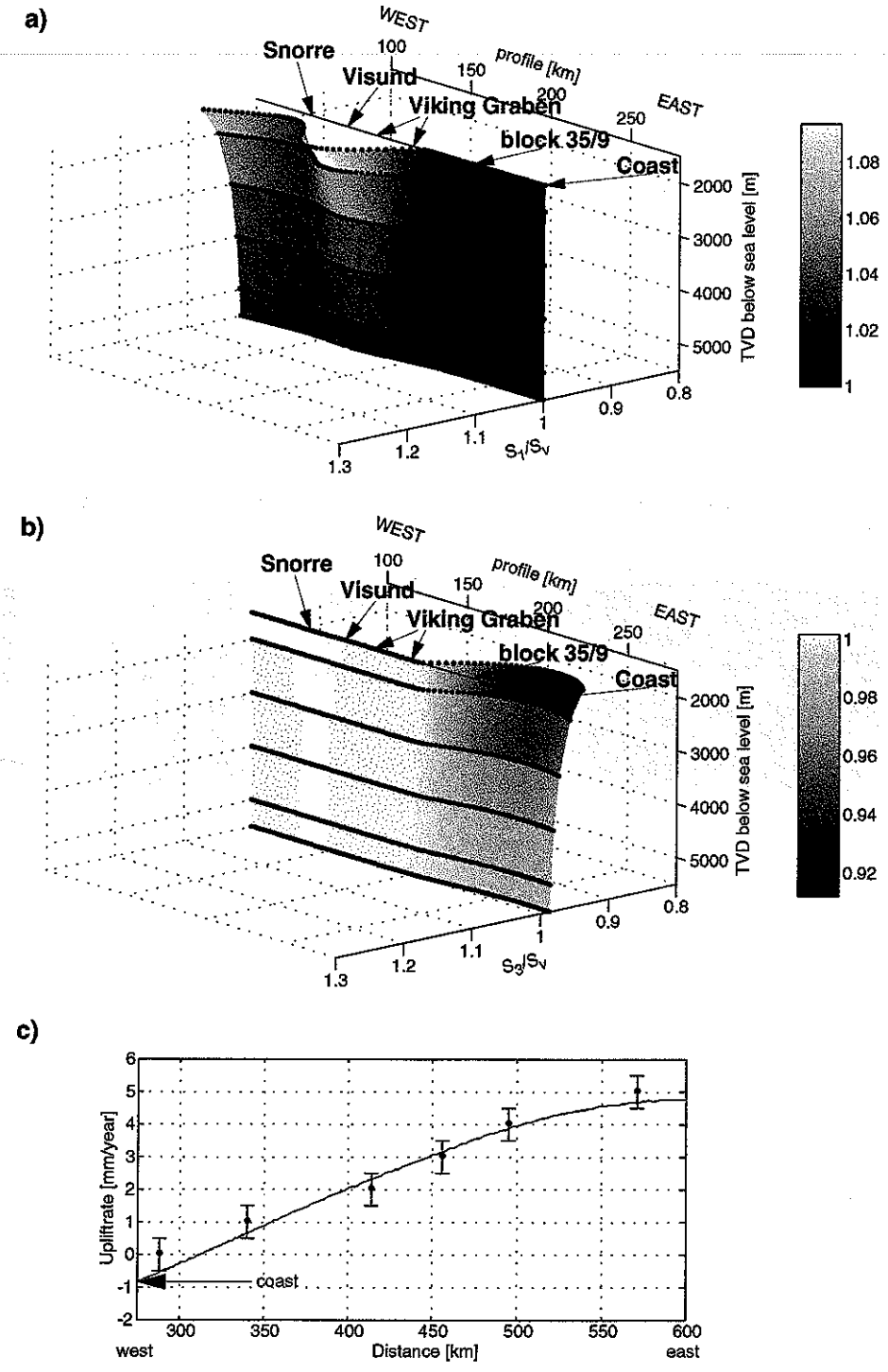
a)
WEST
Snorre
Visund
Viking Graben
block 35/9
Coast
EAST
profile [km]
100
150
200
250
2000
3000
4000
5000
TVD below sea level [m]
1.08
1.06
1.04
1.02
1
0.9
0.8
1.1
1.2
1.3
b)
WEST
Snorre
Visund
Viking Graben
block 35/9
Coast
EAST
profile [km]
1
0.98
0.96
0.94
0.92
c)
Upliftrate [mm/year]
coast
west
Distance [km]
east

Figure 9

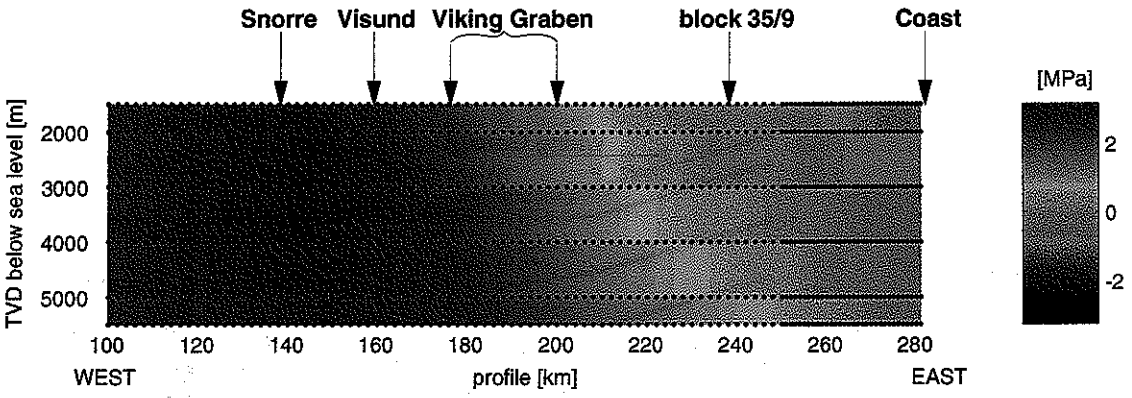
Snorre
Visund
Viking Graben
block 35/9
Coast
[MPa]
2
0
-2
TVD below sea level [m]
2000
3000
4000
5000
100
120
140
160
180
200
220
240
260
280
WEST
profile [km]
EAST

Figure 10